Highly thermal conductive graphene-based heatsink tailored for electric propulsion SiC-based inverter

Downloaded from: https://research.chalmers.se, 2025-12-04 23:43 UTC

Citation for the original published paper (version of record):

Amirpour, S., Orbay, R., Thiringer, T. et al (2024). Highly thermal conductive graphene-based heatsink tailored for electric propulsion SiC-based inverter. Applied Thermal Engineering, 243. http://dx.doi.org/10.1016/j.applthermaleng.2024.122548

N.B. When citing this work, cite the original published paper.

research.chalmers.se offers the possibility of retrieving research publications produced at Chalmers University of Technology. It covers all kind of research output: articles, dissertations, conference papers, reports etc. since 2004. research.chalmers.se is administrated and maintained by Chalmers Library

(article starts on next page)

Applied Thermal Engineering 243 (2024) 122548

Contents lists available at ScienceDirect

Applied Thermal Engineering

journal homepage: www.elsevier.com/locate/ate

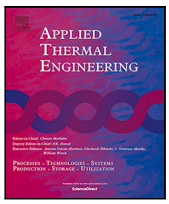

Research Paper

Highly thermal conductive graphene-based heatsink tailored for electric propulsion SiC-based inverter

Sepideh Amirpour [a,c,*], Raik Orbay [b,c], Torbjörn Thiringer [b,c], Majid Kabiri Samani [d], Georgios Mademlis [b], Daniel Larsson [b], Andreas Andersson [e]

[a] Department of Vehicle Electronics & Software, China Euro Vehicle Technology AB, SE-41755, Gothenburg, Sweden
[b] Volvo Car Corporation, Torslanda PVÖS22, SE-40531, Gothenburg, Sweden
[c] Chalmers University of Technology, Department of Electrical Engineering, Division of Electric Power Engineering, SE-41296, Gothenburg, Sweden
[d] Volvo Trucks, SE-40508, Gothenburg, Sweden
[e] InfiMotion Technology Europe AB, SE-41755, Gothenburg, Sweden

ARTICLE INFO

Keywords:
Graphene assembled films
Conjugate heat transfer
Thermal management
Liquid cooling
SiC MOSFET
Electric drives
Electrified vehicles

ABSTRACT

This study introduces an innovative multidisciplinary design approach for highly conductive and lightweight pin-fin-based heatsinks leveraging the advantages of graphene technology. The primary objective is to optimize the thermal management of silicon carbide (SiC) based inverters within electric vehicles (EVs). To closely emulate the real SiC power module, comprehensive analyses, including scanning electron microscopy (SEM) and energy dispersive X-ray spectroscopy (EDS), are performed on the module. A detailed fluid dynamics model utilizing a 3D-conjugate heat transfer (CHT) methodology is employed to evaluate the thermal behavior of SiC power switches in contact with the coolant. The multidisciplinary analysis is initially implemented on an aluminum-based heatsink, validated experimentally, and subsequently compared to graphene. The integration of graphene in the heatsink design demonstrates notable improvements, including a 24.4 % increase in the heat transfer coefficient (HTC) and a 19.6 % reduction in thermal resistance (sink to fluid) at a 6 l/min fluid flow rate compared to its aluminum counterpart. Consequently, the SiC chips within the graphene-based heatsink exhibit an 11.5 % lower temperature rise compared to the aluminum version. The improvements in the cooling solution for SiC inverters in EVs, achieved through the adoption of graphene instead of traditional metals, serve as a proof of concept. This signifies a step forward in prioritizing the crucial balance between performance and power density.

1. Introduction

The design of reliable and efficient propulsion inverters for electrified vehicles within constrained cost and weight parameters poses a significant challenge. In particular, the advancement of switching devices, one of the reliability–critical components towards miniaturization such as gallium-nitride (GaN) and silicon-carbide (SiC) MOSFETs, impose higher temperature stresses that significantly threaten the performance and lifetime of power electronic devices including inverters. Wide-bandgap (WBG) technologies – GaN and SiC switching devices – have recently become prominent in electrified powertrains due to their higher voltage, higher frequency capabilities, as well as smaller die size, compared to Si IGBTs. Nevertheless, despite their inherent advantages, higher current density capability, coupled with higher thermal conductivity, leads to higher temperature variations particularly in SiC MOSFETs. This is contrary to the growing demand for reliability and cost constraints.

One way to cope with these issues is to optimize the thermal conditioning systems prescribing effective heat transfer strategies. Aiming for these strategies, recent efforts have been directed towards researching the potential of novel heat-spreading materials [1,2]. Integrating these materials with ultra-high thermal conductivity can thus substantially lower the operating temperature of the system, accordingly, reducing the temperature stresses on the switching devices [3].

Compared to metallic materials, graphene, a novel heat-spreding material, possesses a superior in-plane thermal conductivity up to (5300 W/m.K) at room temperature [4], far higher than that of copper, (402 W/m.K) and aluminum, (237 W/m.K), [3,5] as well as lightweight property of (2.2 g/cm^3) and good stability [1,3,6]. Specially, compared with a single layer graphene, the graphene assembled films (GFs) have attracted much attention due to their promising potential of heat dissipation performances [3,6].

* Corresponding author at: Department of Vehicle Electronics & Software, China Euro Vehicle Technology AB, SE-41755, Gothenburg, Sweden.
E-mail address: sepideh.amirpour@chalmers.se (S. Amirpour).

https://doi.org/10.1016/j.applthermaleng.2024.122548
Received 12 September 2023; Received in revised form 18 December 2023; Accepted 24 January 2024
Available online 2 February 2024
1359-4311/© 2024 The Author(s). Published by Elsevier Ltd. This is an open access article under the CC BY license (http://creativecommons.org/licenses/by/4.0/).

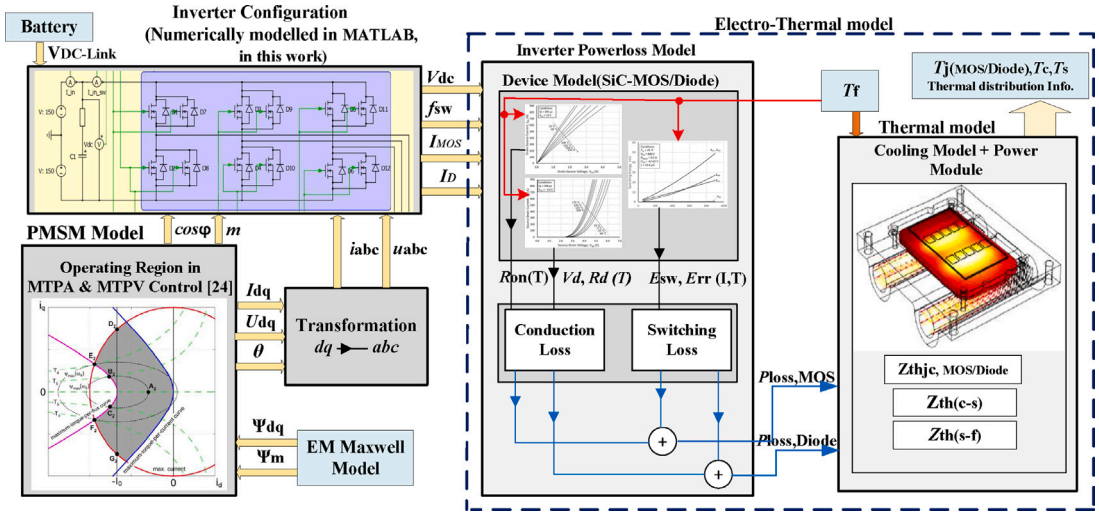

Fig. 1. Inverter's cooling design process overview.

Consequently, different approaches of utilizing graphene as heat spreader for thermal management have been studied and reported in literature for different applications. A new class of graphene enhanced heat pipes are introduced in [6], which dramatically improves the heat dissipation capacity, above that of copper based commercial heat pipes. In [7], a graphene assembled film integrated heatsink with water cooling is used, in which the graphene film was attached to the surface of a Li-ion battery to achieve efficient cooling of a propulsion battery in electric vehicles. Another experimental set-up of a graphene-based heatsink, using a cooling fan is demonstrated in [8] to address the overheating issues in power electronics. Further interesting research are presented in [9–13]. However, these applications have a relatively limited scope when incorporating graphene into their design. Moreover, they do not satisfy the comprehensive aspects of combined electrical, mechanical, and thermal design for a cooling system in a multidisciplinary approach. To the best knowledge of the authors, literature on graphene equipped cooling/heatsinks specifically for power electronic devices is scarce.

In the realm of computational fluid dynamics (CFD), it is a common practice to account for 3-D conduction within the solid layers of semiconductor devices when designing power electronics cooling systems. However, the level of detail in many publications is not explicitly specified. For instance, in [14,15] simulations estimating the temperature of a pin-fin equipped power module are conducted using fins, but without employing conjugate heat transfer (CHT); predetermined heat transfer coefficients (HTC) are used instead. Additionally, in [15], it is mentioned that "a uniform temperature of 25 °C is assumed for the cooling liquid in the heatsink for the simulation", but the fluid, which is in motion over a hot surface, does not seem uniform. The fluid physics, including coolant mixing and natural convection, were not resolved, making the approach less suitable for industrial applications. The conjugate heat solution incorporated an assumed fluid temperature, implying the presence of a stagnant entity. Similarly, in [16], the Flotherm model lacks CFD functionality, relying only on solid conduction. In [17], an electrothermal design of a discrete GaN-based converter for integrated modular motor drives utilizes CFD without CHT. The model does not include metal for the motor, and the fluid is treated as a stagnant entity, an assumed temperature of 20 °C, with no consideration for convection.

Concluding all the above-mentioned context, to the authors' knowledge, neither a comprehensive study has been found in the existing literature that incorporates graphene to enhance the heat dissipation performance of a SiC power module, particularly the overall inverter in EVs, nor utilizes a full CHT approach. Therefore, this study aims to fill this gap employing a detailed CHT methodology in a multidisciplinary process to demonstrate how graphene technology, as a novel heat-spreading material especially in power electronics, can be utilized to challenge existing design techniques and efficiently improve the temperature distribution through the semiconductor module. The study effectively emulates the SiC MOSFETs, modeling them from the chip level down to the fluid, along with the water jacket geometries.

Furthermore, this work demonstrates the possibility of using an open-source software, which is in line with the United Nations sustainability targets [18], especially goals 9 and 10 and aligned with goals 13–15, aims to reduce the CO_2 footprint from the energy conversion system for transport applications, however, the technology can be used for other power electronic applications.

2. Overview of cooling design process for a propulsion inverter

The proposed liquid-cooled heatsink in this study is analyzed following a multidisciplinary approach, to fulfill the design specifications for the next generation of propulsion power converters. The process, depicted in Fig. 1, is designed to address the essential aspects of the inverter's thermal dissipation requirements. It employs a combination of electrical modeling, control algorithms, power loss analysis, thermal and fluid modeling.

This approach is applied to improve the thermal performance of a 3rd generation half-bridge SiC power module, CAB45-0M12X-M3, in the 1200 V class utilized in an electric propulsion inverter. The module has a current rating of 450 A and a capacity of sustaining an operating temperature up to 175°C [19]. Lower switching losses due to faster switching transitions in SiC power modules, as well as lower conduction losses which is particularly achieved by the MOSFET's reverse conduction [20], combined with the capability to operate at higher coolant temperatures make these more attractive than Si-IGBTs. Especially for traction applications where a high ambient temperature can typically be observed, the SiC technology is more beneficial in the design of propulsion inverters [21]. However, as mentioned before, due to higher temperature variations in SiC-MOSFETs especially during aggressive acceleration and decelerations in vehicles, achieving effective thermal management in SiC-based inverters remains a challenge in meeting design specifications. This challenge can be addressed to a noteable extent through the proposed new cooling device assessed by graphene in this work.

As illustrated, the modeled light duty electric propulsion system consists of a permanent magnet synchronous machine (PMSM) including its control. A three-phase 2-level SiC-based inverter and a model of the used SiC-based devices are included. The power loss model of

Table 1
Electric drive parameters.

Parameter	Value	Unit
Current magnitude	400	A-rms
DC-Link voltage	300	V
Blanking time	0.5	µs
Switching frequency	10	kHz
Number of pole pairs	4	–
Torque	160	Nm
Maximum rotor speed	12 000	rpm

the inverter and the proposed heatsink model are added as an electro-thermal model. As the study's objective is to concentrate on the design of a graphene-based cooling tool and its thermal management advantages. Therefore, the detailed technical analysis and mathematical relations of the utilized electrical, control and loss models presented in Fig. 1 are excluded in this paper and can be found in our previous work [20].

Initially, the flux linkage maps, ψ_d and ψ_q, produced in Ansys Maxwell, coupled with the specified electric drive parameters listed in Table 1, are employed to create a PMSM model in MATLAB. The motor control strategies, maximum torque per ampere (MTPA) and maximum torque per volt (MTPV) [22,23] are implemented in a numerical approach in MATLAB. Subsequently, the generated current and voltage reference maps from the PMSM control are then loaded into the inverter and inverter loss model for loss calculations.

The device model in Fig. 1, estimates the voltage drop across the devices, the on-state resistances as a function of temperature, as well as the switching and reverse recovery energies as a function of current and temperature. The coolant temperature T_f, at the inlet is set to 65°C/338 K. Using the inlet temperature, the actual temperature of the chips and accordingly the instantaneous conduction and switching losses of the devices are calculated.

To have an accurate SiC-based device loss determination, as well as a further reduction of the conduction losses, the reverse conduction capability of the MOSFETs is modeled numerically in MATLAB and employed in the inverter loss simulations. Furthermore, the effect of blanking time on the diode's conduction losses is also modeled in the inverter total loss model [20,24].

Finally, the losses calculated based on the inlet temperature are applied to the SiC power module chips, which are emulated and attached to the proposed heat exchange unit for the thermal analysis.

Afterwards, multiple design iterations are carried out, optimizing the heat exchange unit design until both the maximum temperature and the temperature variation at the surface of the heatsink fall within the specified constraints. Worth noting that, the multidisciplinary design process presented here can simulate both the transient and steady-state (constant) thermal performance of the inverter and establish a thorough and highly realistic thermal analysis methodology to assess the performance of the heatsink by introducing grap-hene instead of metallic materials.

3. Liquid based cooling design process for constant heat dissipation

The key objectives for a heatsink design are to enable a uniform heat dissipation while maintaining a low pressure drop balanced with manufacturing, material, and packaging costs. Therefore, the liquid-based cooling with a significantly higher heat transfer coefficient and higher Nusselt number compared to those operating with forced air convection is considered as a better candidate for a high heat flux SiC-based power module.

The heatsink model, which is investigated and optimized in this work, is a type of pocketed folded-Fin cold plate (PFCP) unit, which will make it possible to analyze the significance of graphene on the thermal performances in the following sections, where the material of the heat exchange unit is replaced with graphene.

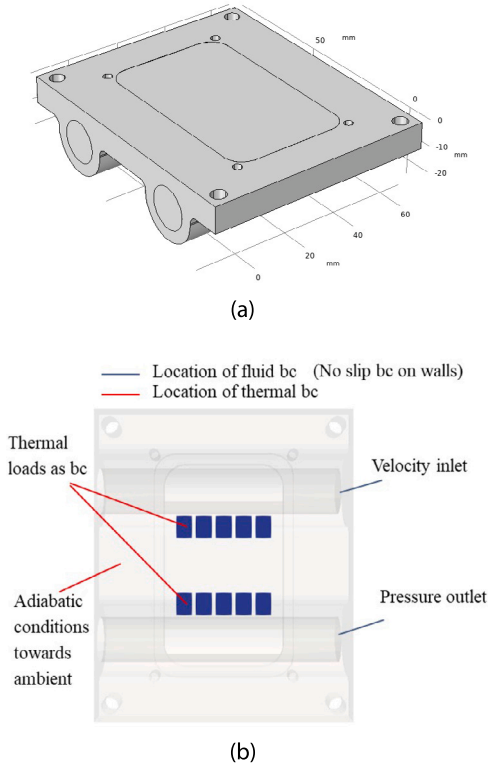

Fig. 2. (a) Geometry of the heatsink, designed for one power module. (b) Locations of the boundary conditions.

In this step, a full transient 3D CHT model of the heatsink starting from a computer aided design (CAD) of the SiC-power module is used, utilizing the software Helyx (an OpenFOAM fork) [25] to study the thermal performance of the module.

To reduce the complexity of the CHT computations as well as to decrease the simulation time, the dimensions of the above-mentioned heatsink are modified to fit a single SiC power module. Consequently, a total power loss of 345 W is calculated for one half bridge module and the heatsink is simulated with constant heat dissipation. The coolant type is chosen as a 50/50 mixture of water and ethylene glycol with volume flows of 1 l/min and 6 l/min, illustrating a practical application in contrast to using pure water alone. Realistic thermophysics of the coolants are often overlooked and instead pure water is used for modeling, which has more cooling ability than the industry-standard glycol mixtures. Fig. 2 visualizes the drawing CAD geometry of the heatsink along with the location of the boundary conditions in a 2D view. The dimensions of the entire heatsink structure, as illustrated in Fig. 2, are 85 mm × 100 mm × 25.5 mm in the x-y-z direction.

3.1. 3D-CAD model and CHT thermal modeling set-up of the power module

In order to provide an accurate model of the heat distribution from the chips in the SiC-devices towards the fluid, a thermal model of the investigated power module is built up with a geometry as close as possible to the real module starting from CAD and then CHT simulation. Although, the thermal packaging aspects of the used module, CAB450, was mostly unknown due to confidentiality, it was at least known that the base plate and insulator have been made of copper and silicon nitride, respectively. Therefore, two experimental analyses consist of a scanning electron microscopy (SEM) along with an energy dispersive X-ray spectroscopy (EDS) were performed on an available

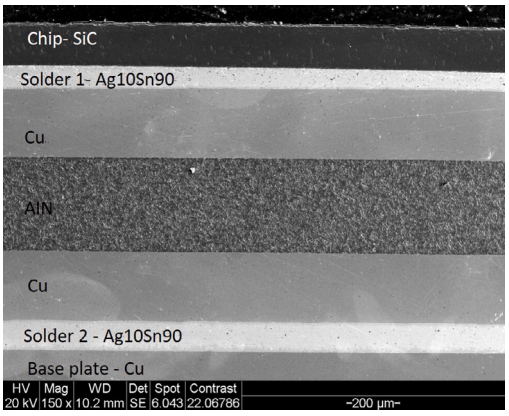

(a)

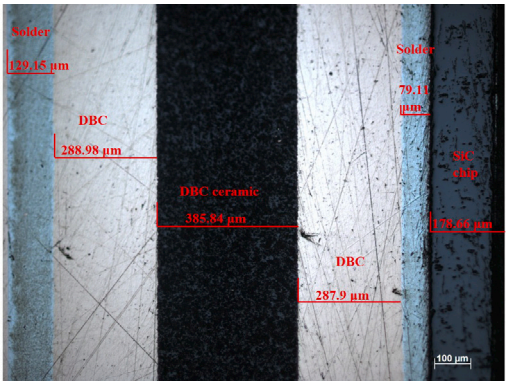

(b)

Fig. 3. Materials and thickness of the reference SiC module CAS300 from SEM and ESD analysis. (a) The Layer materials (b) Materials respective thickness (given in Table 2).

similar voltage class SiC power module, CAS300M12B-M2 [26] as a reference, to approximate further materials information for constructing a realistic thermal model of the module. By conducting these above-mentioned analyses, structures with a very small thickness can be detected. In SEM, the sample is scanned using a highly energetic and focused electron beam, and then an extremely enlarged image of the morphology of the sample can be provided. EDS is a chemical micro-analysis technique, which identifies the X-rays released from the sample throughout a bombardment process with electrons, so that the element arrangement of the analyzed volume can be illustrated [27]. It is worth to note that, the analysis has been conducted on a cross-sectional cut off piece of the module.

As depicted in Fig. 3(a), the chips are all silicon-carbide, the base plate is made of copper and an aluminum nitride insulator has been used as one of the DBC layers. The other two DBC layers are made of copper. Moreover, the SEM/EDS analysis revealed that the solder was $Sn_{90}Ag_{10}$ and it has been used for both solder layers, below the chip and below the DBC layers. The layers respective thickness is presented in Fig. 3(b) and Table 2, along with the material thermal properties.

At this step of the process, the CAD geometry of the investigated CAB450 power module including the thermal aspects is meshed in Helyx, based on the datasheet information and the data provided from the reference CAS300 module. It should be noted that, silicon nitride (Si_3N_4) is used as the ceramic material in the DBC substrate. Fig. 4(a) illustrates a 3D-geometry of the power module in which each group of five chips is representing one SiC switch place in one half-bridge module. The dimensions are implemented according to the datasheet [19].

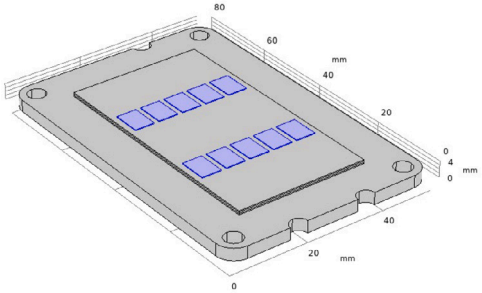

(a)

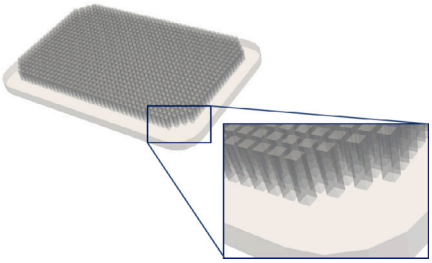

(b)

Fig. 4. (a) 3D-geometry of CAB450 SiC module built for CHT. (b) CAD heat exchange unit.

3.2. Pin fins in water jacket based heatsink

It is reported that the increased surface area and the vortex shedding mechanisms lead to a better heat transfer using rectangular fins compared to using cylindrical fins [28]. The rectangular design, not only increases the heat transfer surface, but also as the separation of the coolant at the edges, it adds additional mixing of the momentum and thermal boundary layers due to vortex shedding on the corners. Conversely, circular pins or other shapes require modeling or special manufacturing processes [29], leading to higher costs and increased complexity. Therefore, from tuning of pin length, width, and distance, an improved heat exchange unit of the heatsink was designed to comprise 1075 rectangular-shaped fins of 1 mm section dimension and 4 mm height in the z-direction as depicted in Fig. 4(b).

This test case provides insights for the prospective use of bundled 2D nanomaterials, particularly critical for EVs cooling. The modeling procedure employed here could be extended to other power-intensive cooling applications.

3.3. Automated CHT computation for steady-state heat dissipation

Implementing fluid–structure interaction modeling, which includes CHT among solids and coolant, as well as among individual solids, provides the most detailed representation of heat transfer from solid to liquid. This approach surpasses the use of simplified representations of solids or a liquid with tuned HTC when determining the heat transferred into the liquid.

The implemented computational steps comprise volume mesh generation on the provided surface meshes, a potential solution to initiate the fluid domain, the CHT run and finally, the data acquisition. The workflow is automatized in order to swiftly account for updates in geometries and/or boundary conditions, enable parameter sweep studies and/or optimization loops. As the resulting mesh for the study is about 40 million finite volume cells, a limited scalability study for various mono- and multi-phase solvers is launched prior to the parallelization to reach the best decomposition set-up, (for example, a ClockTime equals to 11 928 s, for a case that was run on 36 CPUs), resulting in

Table 2
Power module layers' thicknesses and thermal properties.

Layer	Material	Thickness	Thermal conductivity, K (W/m K)	Density, ρ (kg/m^3)	Heat capacity, C (J/(kg K)
Chip	SiC	178 μm	490	3216	690
DBC	Cu	288 μm	400	8940	385
DBC ceramic	Si_3N_4	386 μm	29	3100	700
Solder (below the chip)/(below the DBC layers)	$Sn_{90}Ag_{10}$	79/129 μm	50	9000	150
Baseplate	Cu	3 mm	400	8940	385

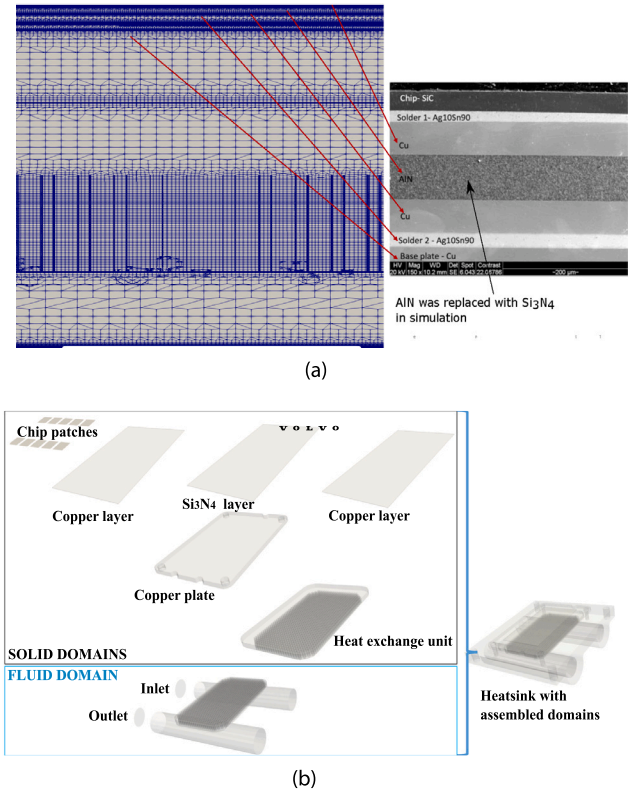

Fig. 5. (a) Computational chip-level mesh modeling of the investigated SiC CAB450M12XM3 module with layers materials. (b) Heatsink unit with assembled domains.

that the 40 million mesh elements for 1000 simulations points were solved in only 3 h. Each computation step of the study is parallelized on 36 to 5832 CPUs, depending on the server load. This allows for minimizing uncertain assumptions and implementing the most accurate physical detailedness which could make the study independent of the subsequent experimental verifications and extended calibration works.

Initial computations using inlet hydraulic diameter showed a developed turbulent field. Accordingly, turbulent mixing is modeled using the k-ω SST model, which provides a good balance between quality and computational time compared to simpler one-/ two-equation models by including shear stress quantification. The Reynolds number field varies between 6300 to 9400 in mid-section for the 6 l/min case using glycol.

To resolve the micron level detail (the Kolmogorov microscale down to 30 μm), the mesh is extensively refined for substrate layers under the chip. Each of the heat sink assembly materials and their thicknesses were accounted for in the meshing procedure, as they were designed as separate computational domains (solder, copper, DBC, etc.) as illustrated in Fig. 5.

In order to take the thermal coupling and heat spreading effects into consideration, the contact resistances among the modeled domains and layers were also modeled using realistic values provided by material datasets. Accurate geometric magnitudes of material layers from X-ray images are also applied for this purpose. So, the lengths clarified from the X-ray imagery are modeled as unique mesh regions with own layer counts, anisotropies, and thermal conductivities. That is why it reached 40 e6 mesh elements, an order of magnitude comparable to full-car aerodynamic simulations. The minimum volume is 6.6e−14 and the maximum 5.42e−10 m3 and the minimum and maximum face areas are 3.57e−10 and 9.65e−07 m respectively. Non-orthogonality, aspect ratio, negative volumes, minimum face areas, etc. are scrutinized to be all OK for OpenFOAM criteria before any computations were launched.

All the thermal anisotropies are handled through directional thermal conductivities. The solution algorithm solves tensors which comprise a Cartesian distribution of heat transfer coefficients for all the materials and is implemented by OpenFOAM. Accordingly, the anisotropy was achieved by implementing the directionality of the thermal heat transfer coefficients particularly in graphene based cooling device.

The utilization of thousands of HPC resources for modeling both the aluminum (Al) and graphene-based heatsinks enabled a detailed examination of vortex shedding on each pin-fin structure, which may be considered unique in the field. The steady-state approach tends to blur the coherent structures related to vortex shedding. Despite running transient cases, vortex shedding persists within the pin-fin cavities among obstructions. This localization of vortices by neighboring pin fins, unlike the von Karman-type free flow, led not to report transient cases representing driving cycles. An alternative option could have involved employing the transient Navier–Stokes equation. However, this would be more time-consuming for only a marginal increase in accuracy, as the vortices are essentially smeared around. Overall, a uniform mesh distribution per domain is aimed for.

In the Finite Volume Method (FVM), the Navier–Stokes equation set, comprising continuity and momentum conservation equations, as well as the energy equation for fluids and solids are discretized over elements in 3 dimensions. By going through the solver script, it can be seen that, $chtMulti - RegionFoam$, the solver from Helyx (an OpenFOAM-based CFD tool), solves the transient equations and for its steady-state variant, the time derivatives are omitted. This solver handles the fluid domain continuity as

$$\nabla \cdot (\rho \boldsymbol{u}) = 0 \tag{1}$$

where $\boldsymbol{u}$ is the velocity vector and ρ is the fluid density. Subsequently, the momentum conservation in the fluid domain is modeled in 3D as [30]

$$\nabla \cdot (\rho \boldsymbol{u}\boldsymbol{u}) + \nabla \cdot (\mu \nabla \boldsymbol{u}) + \nabla \cdot \left(\mu \left[(\nabla \boldsymbol{u})^T - \frac{2}{3} tr\,(\nabla \boldsymbol{u})^T \boldsymbol{I} \right] \right) = -\nabla p + \rho \boldsymbol{f} \tag{2}$$

where $\boldsymbol{f}$ is the body force vector acting on the cooling fluid domain, p is the cooling fluid pressure, μ denotes the dynamic viscosity of the cooling fluid. In (2), the operator tr takes the trace of a tensor in 3 dimensions. The energy exchange among and in the domains is modeled in both domains, in the cooling fluid as [31,32],

$$\nabla \cdot (\rho \boldsymbol{u} h) + \nabla \cdot (\rho \boldsymbol{u} k) = \rho \boldsymbol{u} \cdot \boldsymbol{g} + \nabla \cdot \left(\alpha_{eff} \nabla h \right) \tag{3}$$

Table 3
Properties of the heat exchanger module material.

Material	Thermal conductivity, K (W/m K)	Density, ρ (kg/m^3)	Heat capacity, C (J/(kg K)
Graphene	(x, y, z) = (2900, 14, 2900)	2267	720
Aluminum	237	2700	904
TIM	5	2250	150

where h is the enthalpy of the coolant. k is the kinetic energy of the cooling fluid. The term α_{eff} is the sum of laminar and turbulent thermal diffusivities.

The energy equation is specific for the Finite Volume (volume center data) resolution of the heat transfer differing from Finite Element (vertices data) approaches. This reaches a seamless propagation of the temperature field among fluid and the conjugating solid Finite Volume domains. Finally, the energy equation in the solid domain is modeled as

$$-\nabla(\kappa \nabla T) = 0 \tag{4}$$

where κ is the thermal conductivity of the solid material [33].

4. Graphene material and manufacturing feasibility of graphene based heatsink

As mentioned in Section 1, the electric components can be designed in a more compact fashion if using materials with high thermal conductivity. Graphene is known for its lightweight and excellent heat transfer ability.

Composed of one or a few atomic layers of sp^2 bonded carbon, phonon transfer inside graphene is extremely efficient, which leads to an outstanding in-plane thermal conductivity [3]. However, using a single or a few layer of graphene for thermal management of high power practical applications did not fulfill the expected performance due to different reasons, such as poor quality, non-freestanding structures, complex transfer processes, size limitation, and most of all limited heat flux carrying capacity [3]. Hence, fabricating the graphene films (GFs), assembled from separate graphene sheets, by using process-based graphene fabrication methods, made it possible to reach excellent thermal and mechanical properties of the material [3,34,35]. To meet the final performance in the fabrication process, various critical items should be taken into account. The first factor is the grain size. The GFs composed by individual graphene sheets, contain big amounts of defects that increase the phonon scattering and then limit the thermal conductivity [36]. Alignment is an important second factor that can affect the thermal performance of the GFs. Due to the flexible nature of graphene, it would be very hard to avoid the wrinkles and layer misfits during the film formation. This can be more obvious with the increase in thickness of a GF [37]. The phonon interfacial scattering is the third crucial factor in the fabrication process. The strong binding between the neighboring layers in GFs can result in severe phonon interfacial scattering. This will later lead to a decrease in the thermal conductivity of graphene films [38].

Therefore, overcomig these restrictions and gaining a high in-plane thermal conductivity in fabricated graphene films, is very challenging and still limited in practical studies. The methodology based on a dry-bubbling approach which has been performed in [3] could make it feasible, providing a great value. In this method a strong reduction effect of an aluminum substrate together with extremely high-temperature graphitization (2850 °C) and strong mechanical pressing are utilized to enable the formation of high quality GFs.

Additionally, in the fabrication process, in order to minimize the thermal contact resistance between the graphene layer and other different substrates, a molecular functionalization method is used in which the small molecules are utilized to functionalize the surface of the graphene film which is in contact with the device surfaces. The small molecule, as the functional agent, gives a formation of molecular bridges between the device substrates and the grapheme-based surface and in this way the thermal resistance between these layers is strongly reduced [39].

Consequently, using graphene films in heatsink manufacturing, particularly shaping the films in a certain way to make the pin fins, cannot be easily achieved in standard electronics labs. As mentioned in Section 1, some experimental set-up of graphene composed cooling campaigns have been performed in previous studies [7,8,40]. Nevertheless, given the importance of the above-mentioned fabrication factors, the manufacturing process seems to be quite limited and not detailed.

Therefore, in this work, CHT was found to be a reliable method to investigate the effect of the material choice on the thermal dissipation power and compare this with aluminum.

4.1. Modeling of graphene pin fins in the heatsink

To model the graphene-based heatsink, the heat exchange unit, including the cold plate and pins, is constructed using graphene. To create the pins, a 1 μm thick graphene films with in-plane thermal conductivity of 2900 W/mK in x and z direction and a cross-plane thermal conductivity of 14 W/mK in the y direction have been chosen and assembled to make a 1 mm section dimension of the pin fins.

As mentioned in Section 4, the thermal conductivity levels are very much dependent on the thickness of the layer. The lower thickness, the higher thermal conductivity [3]. Therefore, the trade-off between the thermal conductivity and the thickness of the films should be precisely taken into account in the design specification.

Moreover, the proposed heat exchange unit is to carry the heat in the principal direction between the chips and the coolant. Therefore, aligned with the flow through the pins, the x direction is the second important heat transfer route as a design parameter for the graphene heatsink. Table 3 depicts the thermal properties of graphene, aluminum and the thermal paste material.

5. Results of CHT computations applied to the designed aluminum and graphene pin fins based heatsinks

As a heatsink material, aluminum is already a good heat conductor. Unless aimed for manufacturing, the thermal conductance is the same in every direction and there are no anisotropies in the material. On the contrary, for the graphene cooling device, all material anisotropies should be addressed through directional thermal conductivities, achieved through the detailed CHT model in this work.

First, the aluminum heat exchange unit in the modular heatsink assembly is appropriately positioned immediately under the chips. The thermal interface material (TIM), has been chosen with the thickness of 75 μm to better represent the thermal coupling between the power module and the heatsink. Accordingly, the heat transfer to the surfaces of the heatsink, at the reference temperature of 338 K for two different fluid flow rates of 1 and 6 l/min are measured. It should be noted that, the heatsink is exposed to a heat energy injection of 34.5 W power loss per chip.

After modeling the graphene-based fins, for a fair comparison, similar CHT computation steps as for the aluminum-based heatsink were performed. Fig. 6 illustrates the streamlines in the fluid domain as well as the top view of the xy surface including the chips. It can be observed that, the coolant flow is accelerated more among the pins under the module, indicating effective and rapid heat dissipation from the area towards the outlet, as expected. That means, the highly conducting graphene material helps the in-plane heat spreading and makes a uniform temperature profile over the module down to the coolant.

The immediate effect of the graphene material reflects itself also in the heat transfer coefficients for the heat transfer surfaces as presented in Table 4 at the reference temperature of 338 K. As it can be

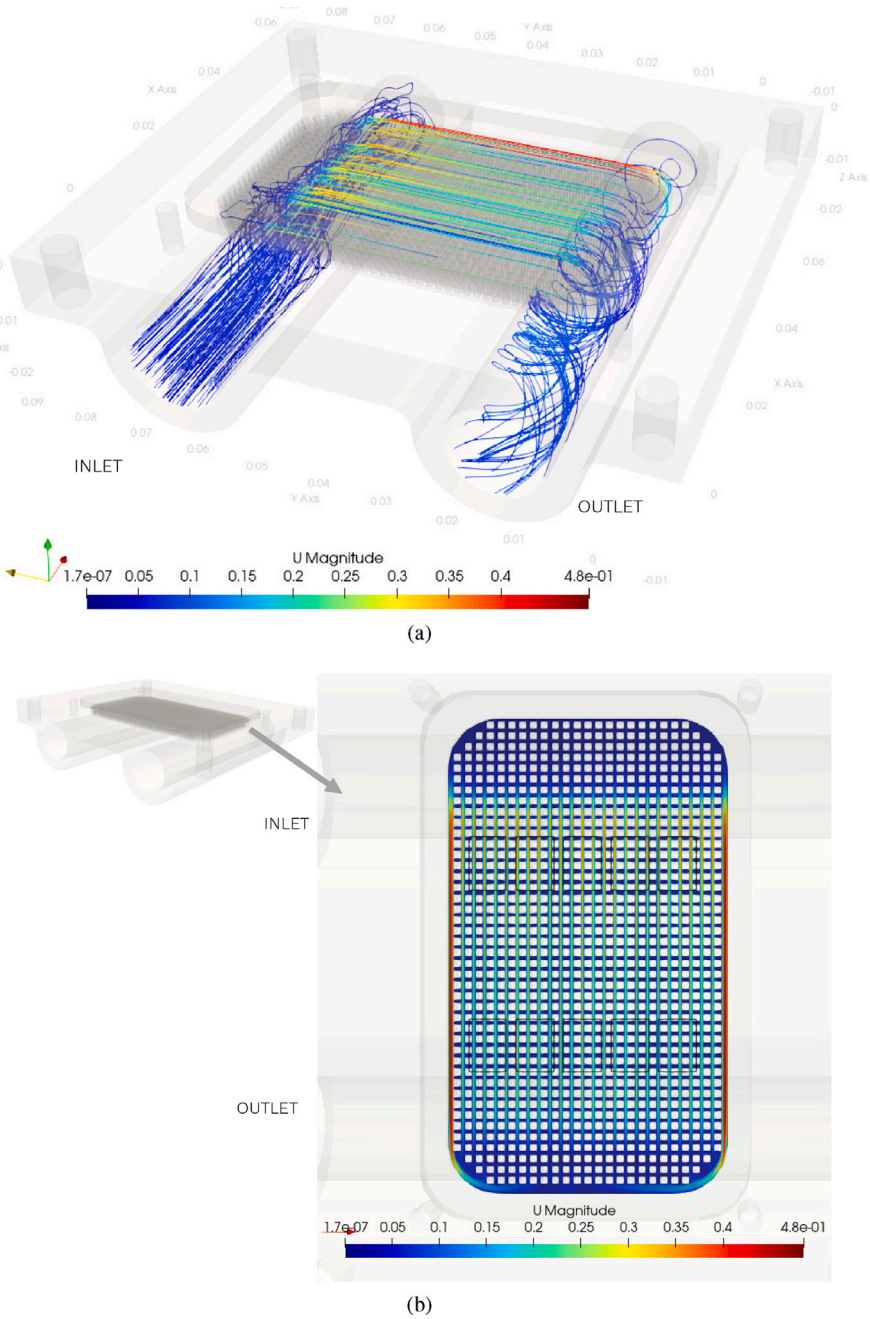

Fig. 6. CHT computation in graphene-based heatsink (a) Streamlines in the fluid domain. The triad colors red, yellow, green corresponds to axes directions x, y, z, respectively. (b) Top view of the xy surface including the chips highligted feature edges in black.

Table 4
Results of heat transfer to the surfaces of both the Al./Gr. heatsinks.

Heat transfer to the surfaces of the heatsinks	Coolant flow rate (l/min)	Convective heat flux (W)		Wall temp. (K)		Twall-Tref. (K)		Convection heat transfer coefficient (HTC) (W/m^2 K)	
		Al.	Gr.	Al.	Gr.	Al.	Gr.	Al.	Gr.
Glycol to Al./Gr. heat exchange surface	1	279.86	284.01	345.7	345.54	7.7	7.54	1962.68	2034.4
	6	275.4	280.98	340.67	340.19	2.67	2.19	5572.5	6930.64

seen, the results are including the convective heat flux, the difference between the wall and the reference temperatures and the convection heat transfer coefficients for the two different flow rates.

According to the CHT computation values for the graphene heatsink given in Table 4, the heat transfer coefficient of the graphene heatsink shows an improvement of 3.65% for 1 l/min and a substantial value of

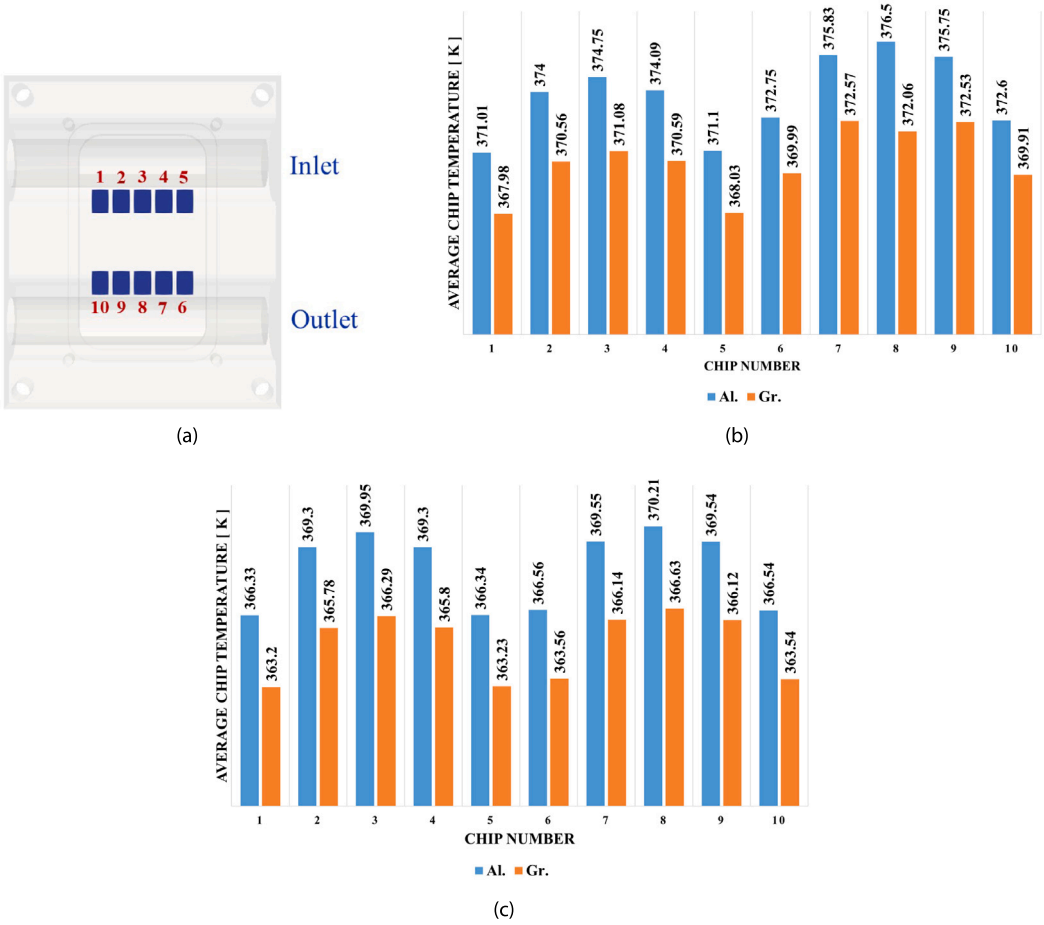

Fig. 7. Chip numbers and average temperature of the chips in the aluminum and graphene heatsinks. (a) Chip numbers. (b) Aluminum vs graphene at 1 l/min fluid flow rate. (b) Aluminum vs graphene at 6 l/min fluid flow rate.

24.4% for 6 l/min compared to those of the aluminum counterpart. Moreover, the simulation with graphene indicates a decrease up to 3.7% for 1 l/min and 19.6% for 6 l/min in the calculated thermal resistance between the cooling plate and the coolant fluid, $R_{\mathrm{th-sf}}$.

Furthermore, as depicted in Fig. 7, the average temperature of the chips for both the aluminum and graphene heatsinks were calculated for 1 and 6 l/min coolant flow rates. As illustrated, all the average chip temperatures are lower for the graphene than that for the aluminum heat exchange unit for the same coolant flow. For instance, considering the chip number 8, for the applied thermal load of 34.5 W per chip and a 1 l/min fluid flow rate, the chip temperature with respect to 338 K (reference fluid temperature), increases of 38.5 K for the aluminum unit and 34.06 K and for the graphene one, i.e., the chip temperature in the graphene unit is cooled down to 11.5% compared to that in the aluminum one in relation to the cooling fluid.

However, the most significant contribution of the graphe-ne insertion observed in this work is a substantial improvement in the speed of heat dissipation from the surface of the chips towards the fluid. Fig. 8 presents how the heat is absorbed from the chip level layers and rapidly distributed further to the liquid via the graphene fins compared to that of the aluminum ones.

The reason behind the observed enhancements in thermal performance of the graphene cooling device could be expressed as the high in-plane thermal conductivity and thermal diffusivity of graphene films (in z-direction), could significantly boost the heat conduction speed through the different material layers. Furthermore, the heat is spreading over a larger volume and more homogeneously in each layer (in x-direction), which means that each layer is absorbing the heat uniformly, leading to a more uniform temperature profile for the heat convection cooling. Accordingly, through the better spreading, the thermal resistance goes down, since more of the heatsink is utilized for heat conduction. Hence, the in-plane heat spreading speed as well as the temperature uniformity leads to an improved heat dissipation ability.

Moreover, as heat transfer via convection reads,

$$Q = h \cdot A \cdot \Delta T \tag{5}$$

where A, the geometry of both cooling devices is similar and the heat transfer coefficient, h, is fixed (fluid remains the same), the change in ΔT is what facilitates a higher thermal dissipation power. As previously discussed, turbulent mixing is effective in dissipating heat, but it needs efficient heat transfer on the other side of the continuum. In the case of aluminum, the limited thermal conductivity acts as a bottleneck. The use of graphene material enhances heat transfer, significantly overcoming the bottleneck imposed by aluminum's limited thermal conductivity. Consequently, this improvement enables the turbulent mixing process to dissipate higher thermal powers.

5.1. Life cycle impact and power density comparison: Graphene vs. Aluminum cooling

As mentioned before, graphene in addition to its high thermal conduction advantage, possesses a lightweight property of 2.2 g/cm^3 [1,3]. This results in improvement of the overall system efficiency, as the vehicle is used in different speeds and accelerations through its lifetime. To discern the advantage of the graphene heat exchange unit from a life cycle analysis perspective, a system study has been set up, using a standard lumped parameter vehicle system performance software

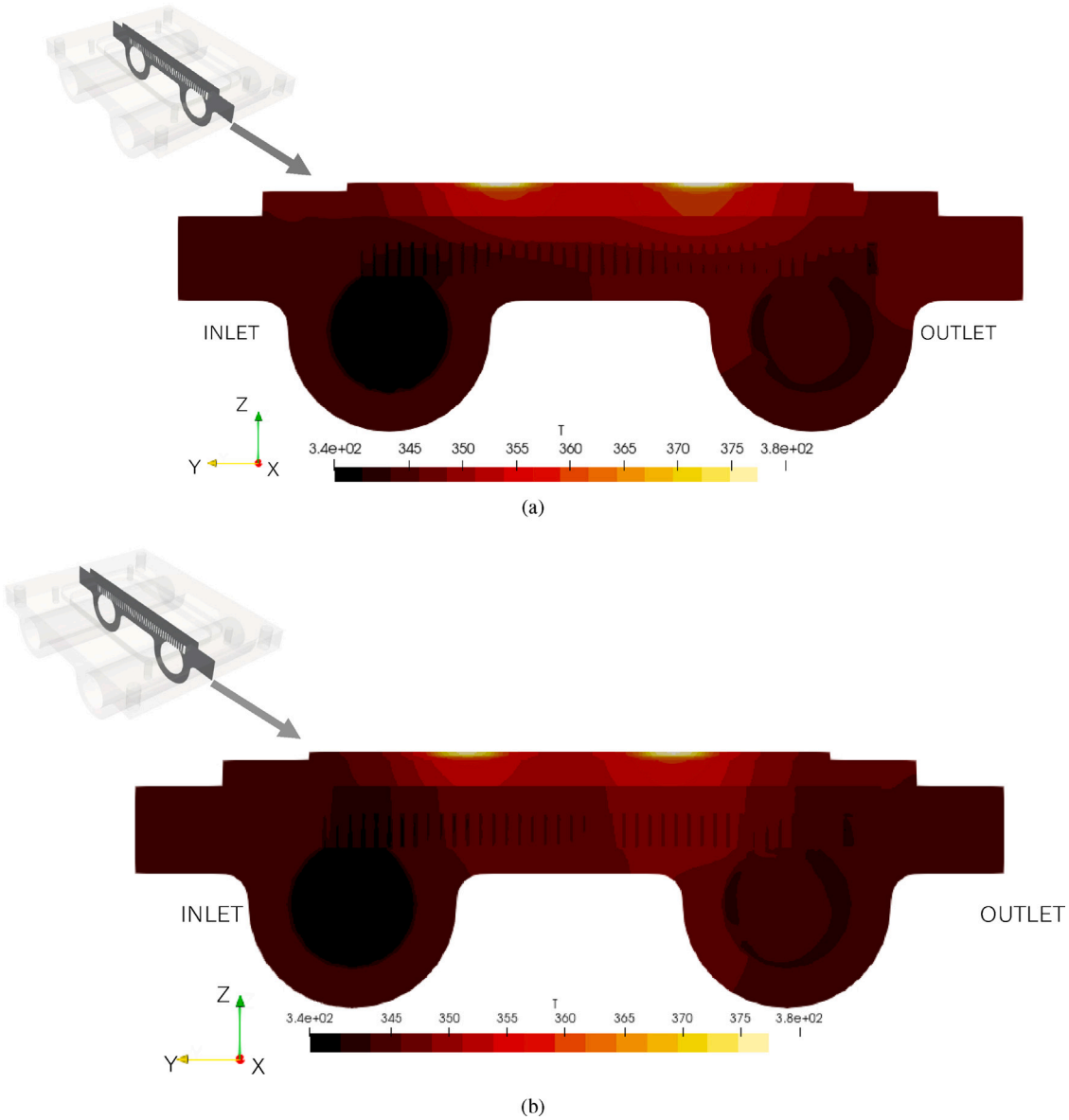

Fig. 8. Steady-state temp. distribution in the heatsinks at 1 l/min.(a) Aluminum heatsink. (b) Graphene heatsink.

commonly used by the OEM. The mass of the heat exchange units was computed based on the mass density of 2712 kg/m^3 for aluminum and 2267 kg/m^3 for the graphene unit, using the CAD software, then tested for CO_2 emissions in two vehicle simulations. The calculation showed a mass of 0.03715 kg for the aluminum unit and 0.03105 kg for the graphene one, which is 16.4% lighter than that of the aluminum one. Moreover, the calculated power density of the heat exchange units, presented a higher value up to 1.55% for the graphene heat exchange unit compared to the aluminum one. For the system study of the life cycle analysis, a C-segment BEV with two electrical propulsion units is used, comprising two full size inverter cooling jackets, positioned on the front and rear axles. In the first simulated vehicle, the inverters were cooled using the aluminum heat exchange units and the second vehicle using the graphene made units. The vehicles were run on a charge depletion cycle based on repeated Worldwide Harmonized Light Vehicles Test Procedure (WLTP) cycles.

The system computations for the complete lifetime of the BEV (400 000 km), gave an energy saving of about 4 kWh for the graphene unit with the mass of 0.0061 kg lighter than the aluminum one. It means, based on EU figures for electricity mix in 2017 (294.206 gCO_2 /kWh) [41], this corresponds to a reduction of about 1.2 kg CO_2 per vehicle for 400 000 km.

5.2. Impact of thermal contact resistance on chip temperature

As previously stated, thermal contact resistances are incorporated in this study, with a calculated thermal contact of 0.035 K/W between the solder layer and chips as well as a value of 0.0037 K/W between the solder and DBC layer, included in the computational tools. A significant difference has been observed on the chips temperatures when ignoring the contact resistances compared to the case with incorporating the thermal contacts in the model. Fig. 9 illustrates the chips temperatures for the graphene heatsink exposed to a liquid flow of 1 l/min when ignoring and not ignoring the thermal contacts of the solder layer with the chips as well as the solder with the DBC layer. A comparison between the temperatures of the first chips from the inlet side, (chips 5 & 6) shows that, the temperature went down from 368.03 K to 361.82 K, i.e. a decrease in chip's temperature rise (with respect to the inlet temperature) from 30.03 K to 23.82 K, i.e 20% lower when ignoring contact resistances, which is indeed substantial.

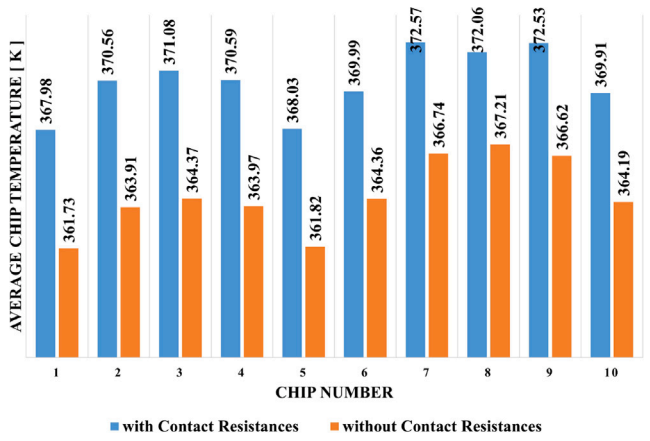

Fig. 9. Temperatures of chips measured at 1 l/min in the graphene heatsink, considering and not considering the contact resistances between the solder layers and material layers in SiC module.

6. Validation of implemented CHT method

To assess the accuracy and comprehensiveness of the implemented CHT simulation setups in this work, various evaluations were conducted and followed through experimental verification, as detailed in the following subsections.

6.1. Simulation assessments

As outlined in Section 3.3, the design took into account the specifics of vortex shedding on each of the pin-fin structures, contributing to the enhancement of thermal performance. Heat transfer in high Reynolds number flows is governed by turbulent mixing. Turbulence arises from the cascading process of eddies, wherein the momentum of the coolant flow is distributed across various wavelengths of the turbulent flow structures. Vortex shedding is the phenomenon where the coherent structures formed during the energy cascade process in the coolant fluid flow eventually transition into turbulence, thereby enhancing mixing. This is crucial for precise modeling.

In Fig. 10, observers are positioned in the wake of an individual pin with a 1 mm edge length. The plotted line colors present the flow speed as shown in the legend. The tangent vectors of these streamlines represent the velocity vector field of the flow, indicating the instantaneous direction of the flow field. The visualization shows that the computational detailing in this design captures enhanced vortex shedding, which clearly contributes to accurate modeling of the mixing of cold and hot cooling fluid regions within the coolant media.

This level of detailing, often overlooked, and the convection flows are typically lumped into a heat transfer coefficient. Notably, the creation of a low-pressure vortex zone behind each pin, indicating that the model captures the micron scale (the Kolmogorov microscale down to 30 μm). Accordingly, the precise dimensions and positions of these vortices, play a crucial role, are modeled for each individual pin on the heat transfer unit. Rather than relying on an assumed overall heat transfer coefficient for the unit, the heat rate is computed for each micron-sized mesh element.

To assess the significance of employing a full CHT implementation versus a CFD using a predetermined HTC, an aluminum pipe with a total wetted area of 0.03 m^2 was utilized for cooling. Conducting the convection balance for 10 chips, applying 34.5 W power on each as heat sources, a lumped parameter cooling computation approach, using Eq. (5), was employed, (345 W = HTC * 0.03 m^2 * 7.7 K), which gives an HTC value of 1494 ($W/m^2.K$), whereas the 3D-CHT computed value, as indicated in Table 4 is– 1962.68 ($W/m^2.K$). Consequently, the junction temperature increase versus the cooling media would be only 5.85 K, considerably lower than the computed 7.7 K mentioned in the table.

Evidently, the assumed HTC for the utilized pipe affects the results compared to employing a full CHT, which calculates an average HTC for all the cells.

In the next step of the simulation assessment, the conventional lumped parameter model (LPM) method is compared with the implemented CHT method in determining the hotspot temperatures over each individual chip.

An equivalent Cauer thermal model was built in MATLAB using Simulink/Simscape to investigate the heat transfer through each individual layer of the power module down to fluid. The model considered thermal coupling and the heat spreading effect at a 45° angle, accounting for realistic thermal resistance and capacitances of each layer. The calculations utilize parameters derived from SEM and EDS analyses, as outlined in Table 2. It is worth noting that the aluminum cold plate, including the pinfins, was integrated into the Cauer thermal model. The result is illustrated in Fig. 11.

As evident, the hotspot temperature is 5 Kelvin higher than what the LPM method would predict, indicating a 14% higher temperature increase. This underscores the detailed capability of the current study in determining the hotspot temperatures over each chip, in contrast to lumped parameter network studies.

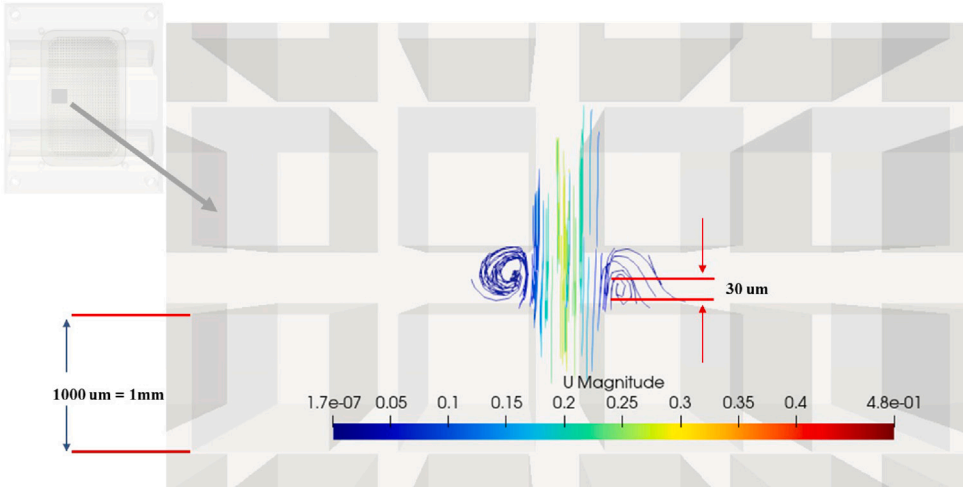

Fig. 10. An enhanced vortex shedding captured by the computational detailing.

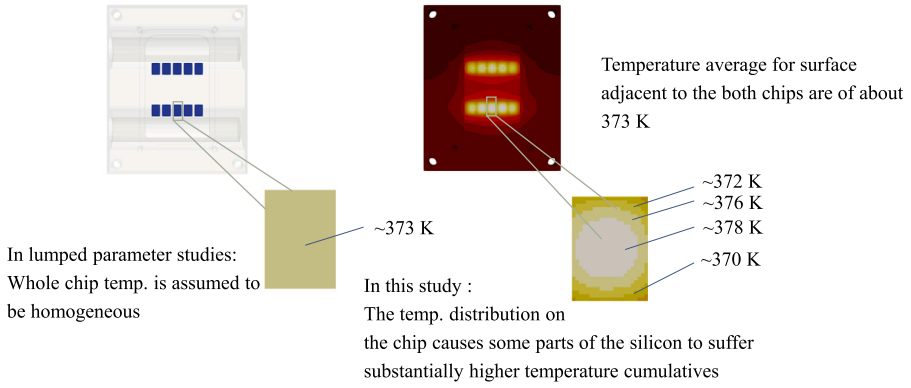

Fig. 11. Chip temperature investigated in this work at 1 l/min compared with lumped parameter approach.

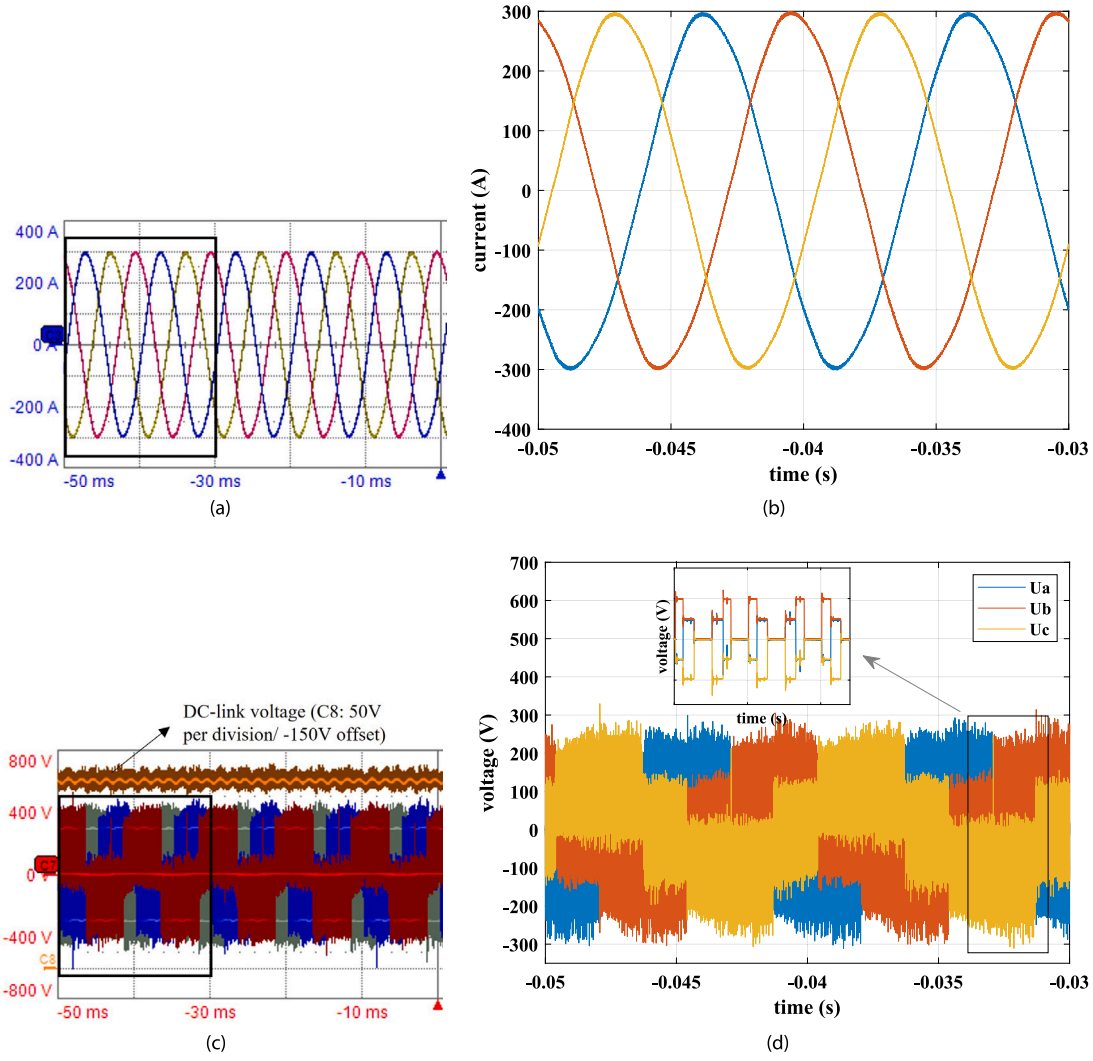

Fig. 12. Selected boundary conditions in the experiment and simulation. (a) Three phase currents. (b) A zoomed-in view of the currents. (c) DC-link and instantaneous voltages. (d) A zoomed-in view of the voltages.

6.2. Experimental validation of implemented CHT on the designed aluminum heatsink

As expressed in Section 4, at the moment the fabrication of the graphene assembled films utilized in the proposed graphene heatsink design is very challenging for standard electronics lab. Hence, in order to verify the operation of the proposed modeled heatsink, the available aluminum one is used on a test bench that includes two identical SiC-based inverters. One of the inverters is the load inverter and the other one acts as a Power-Hardware-in-the-loop system, emulating an electrical machine (the details can be found in our previous work [42]). Selecting a 300 V inverter DC-Link voltage, 300 A current and 25 kHz switching frequency, the total power loss of 1401 W corresponding to a 180 Nm/ 1500 rpm operating point of the machine emulator has

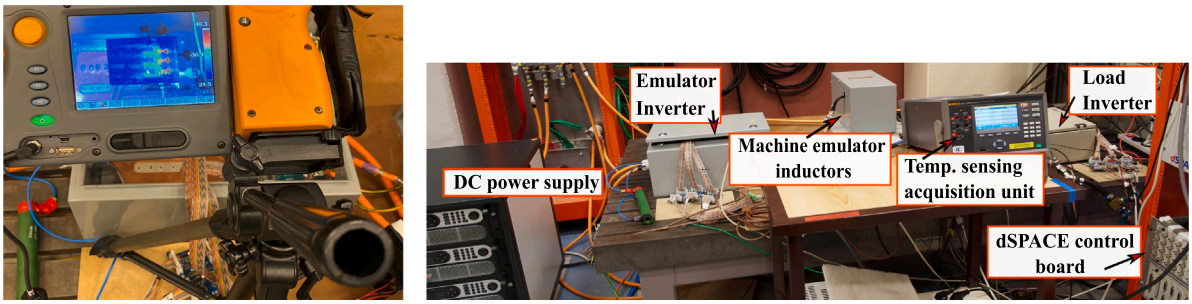

Fig. 13. (a) IR-Camera setup on the SiC power module of the inverter. (b) Test setup.

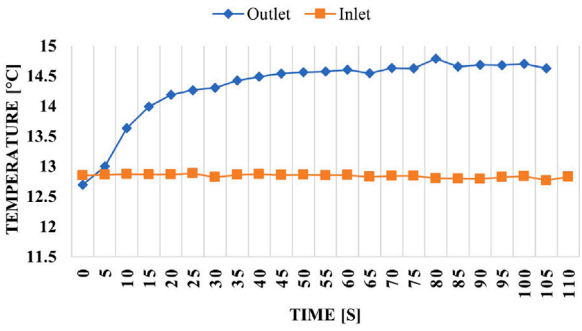

Fig. 14. Experimentally observed temperature profiles of inlet and outlet.

been applied to all the three CAB450 SiC modules, i.e., 46.7 W per chip. Fig. 12 illustrates the DC-link voltage, three phase currents and instantaneous voltages used in the experiment.

Water at 12.85°C/ 285.85 K with a flow rate of 6 l/min has been used as coolant. To observe the temperatures of the inlet, outlet, and four spots on the surface of heatsink, 6 PT-100 sensors were installed at relevant sensing points. More specifically, 2 sensors were positioned inside the inlet and outlet, respectively, close to the wall and the remaining 4 sensors were located as close as possible to the location of SiC power module on the aluminum surface of the heatsink. An infrared thermal camera was also used to observe the temperature distribution over the SiC module. Fig. 13 illustrates the test setup.

The thermal interactions caused by the losses of the SiC-inverter were thus evaluated by using the proposed heatsink design. In order to compare the experimental results vs simulation, the CHT simulation has been run with the same boundary conditions as in the experiment. Fig. 14 depicts the experimental temperature profiles of the inlet and outlet. The temperatures were registered from the CHT simulation with probes located at the same locations as in the experiment. As can be observed from the figure, the steady-state temperature of the outlet is about 14.6°C. This corresponds well to the value of 14.1°C obtained from the simulation for the corresponding probe location. It is worth noting that, in the experiment, the inner layers both in the power module and the designed heatsink is not easily accessible, most of the valuable information obtained in the simulation is hard to measure in the test setup through the sensors or the IR camera.

Following, the position of the other 4 sensors located on surfaces of the heatsink and the respective temperature profiles are illustrated in Figs. 15(a) and (b).

According to Fig. 15(b), the sensor temperature profiles are stabilized at a temperature close to 18.8°C, i.e., a temperature rise ΔT of about 6 °C with respect to the inlet temperature. The steady-state temperature rise obtained from both the experiment and the CHT simulation are given in Table 5. As can be seen, the observed steady-state temperature rise in the experiment has a deviation of around 0.5°C / 10% from the corresponding values in the simulation which is considered to be a good agreement. The given R_{dsON} in the semiconductors for 25°C has a span from typical 2.6 mOhm to a maximum stated value of 3.7 mOhm, from the datasheet, and we utilized the typical value. Furthermore, the contact in particular between the solder and other layers is also uncertain. And of course the outer conditions like flow of air, etc., are also hard to get identical.

All in all, the experimental thermal distribution in the aluminum modeled heatsink proved to be in a moderate accordance with the simulation results regarding to thermal performance. Accordingly, the proposed design method is proved for the modeling of the graphene-based heatsink.

7. Conclusion

An accurate 3D-CHT computation of a lightweight and highly efficient heat spreader liquid-cooled heatsink for a SiC-based power module (utilized in an electric propulsion inverter) has been modeled, employing graphene technology which is a novel heat conducting material especially in power electronics. The detailed 3D-CHT modeling of the heatsink, employed through a multidisciplinary approach encompasses all relevant physics in the simulation and avoids assumptions on HTC or constant temperature. It establishes a precise tool capable of comprehensively addressing all thermal and fluid-mechanical requirements of the proposed graphene heatsink. This methodology contrasts with other applications in the literature, which were constrained by limited design and scope.

The study demonstrates a substantial improvement of 3.65-% and 24.4% in the thermal transfer coefficients for a 1 l/min and 6 l/min fluid flow rate, respectively, compared to those of the aluminum heatsink. This facilitates a rapid and more efficient heat conduction through the material layers from the chips to the liquid, leading to reduced thermal resistances (19.6% for 6 l/min fluid flow rate) between the cooling plate and the coolant fluid. Consequently, this lowers the temperatures per chip (11.5%) in comparison to those in the aluminum counterpart.

Accordingly, in the multidisciplinary procedure presented here, the crosstalk design process of electrical and thermal aspects can be formulated so that a homogeneous temperature distribution in the designed graphene heat exchange unit has been fulfilled, which is strongly governing the chips' lifetime. In fact, this homogeneous temperature distribution tunes a cooling power to minimize the temperature variance per chip. This accomplishment translates into a cascade of benefits, including reduced overall system temperature, the prolongation of system lifetime, an extended drive range, a lighter cooling system, enhanced performance and sustainability of the power electronics system.

Overall, this work is a first proof of concept for a potentially more efficient cooling solution for inverters in electrified vehicles, generally in lightweight applications, in automotive and/or aeronautics, where the trade-off between performance and power density is of the utmost importance.

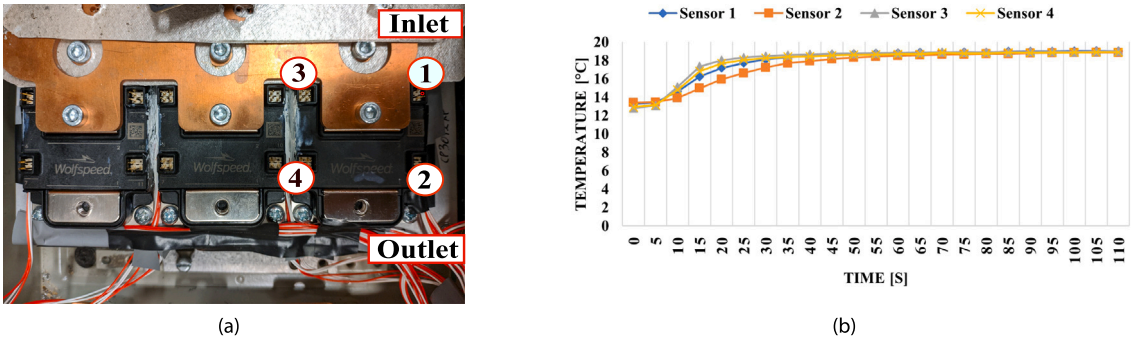

Fig. 15. (a) PT-100 sensors located on the surfaces of the heatsink around the SiC power module . (b) Experimentally observed temperature profiles of the sensors.

Table 5
Steady-state temperature rise of the sensors from simulation and experiment.

	Steady-state temperature rise respect to the inlet/reference temperature			
	Sensor No. 1 temperature rise ΔT_1 [°C]	Sensor No. 2 temperature rise ΔT_2 [°C]	Sensor No. 3 temperature rise ΔT_3 [°C]	Sensor No. 4 temperature rise ΔT_4 [°C]
Simulation	5.23	5.09	5.49	5.43
Experiment	5.72	5.41	6.14	5.93
Diff. [°C]	0.49	0.32	0.65	0.5
Diff. %	9.3	6.2	11.8	9.2

For future work, the primary focus would undoubtedly involve the construction of the graphene-equipped heatsink. This entails addressing the manufacturing challenge, specifically developing a method to experimentally integrate graph-ene fins into a copper/aluminum cold plate within the heatsink. Although, the functionalization process mentioned in Section 4, involving the attachment of the graphene layer surface to metals, has been tested and reported in literature [39], it remains imperative to conduct additional experimental validation. Furthermore, the impact of graphene-based heatsink over pressure drop, attributed to the surface roughness of graphene, which may vary from a smooth metal surface (or even a CNC-milled surface), can be experimentally examined in comparison to that of the aluminum heatsink. Moreover, conducting an environmental assessment is essential to verify that the energy savings resulting from the addition of graphene "pay off" in terms of overall sustainability.

However, it is equally imperative to emphasize more theoretical investigations to substantiate the advantages of incorporating graphene in heatsinks and packaging for power electronic applications.

CRediT authorship contribution statement

Sepideh Amirpour: Conceptualization, Methodology, Writing – original draft. **Raik Orbay:** Methodology, Software, Writing – original draft. **Torbjörn Thiringer:** Supervision, Writing – review & editing.

Declaration of competing interest

The authors declare that they have no known competing financial interests or personal relationships that could have appeared to influence the work reported in this paper.

Data availability

The authors do not have permission to share data.

Acknowledgments

The financial support given by the national energy administration, Sweden, Energimyndigheten, Sweden, as well as CEVT, Sweden and Volvo cars, Sweden are gratefully acknowledged.

References

[1] A.A. Balandin, S. Ghosh, W. Bao, I. Calizo, D. Teweldebrhan, F. Miao, C.N. Lau, Superior thermal conductivity of single-layer graphene, Nano Lett. 8 (3) (2008) 902–907, PMID: 18284217.

[2] Y. Fu, J. Hansson, et al., Graphene related materials for thermal management, 2D Mater. 7 (1) (2019) 012001.

[3] N. Wang, M.K. Samani, H. Li, L. Dong, Z. Zhang, P. Su, S. Chen, J. Chen, S. Huang, G. Yuan, X. Xu, B. Li, K. Leifer, L. Ye, J. Liu, Tailoring the thermal and mechanical properties of graphene film by structural engineering, Small (2018) e1801346.

[4] T.M. Tritt, Thermal Conductivity: Theory, Properties, and Applications, Springer Science and Business Media, 2005.

[5] L. Peng, Z. Xu, et al., Ultrahigh thermal conductive yet superflexible graphene films, Adv. Mater. 29 (2017) 1700589.

[6] Y. Liu, S. Chen, et al., A lightweight and high thermal performance graphene heat pipe, Nano Select WILEY (2020) 364–372.

[7] Y. Liu, T. Thiringer, N. Wang, Y. Fu, H. Lu, J. Liu, Graphene based thermal management system for battery cooling in electric vehicles, in: 2020 IEEE 8th Electronics System-Integration Technology Conference, ESTC, 2020, pp. 1–4.

[8] N. Wang, Y. Liu, L. Ye, J. Li, Highly thermal conductive and lightweight graphene-based heatsink, in: 2019 22nd European Microelectronics and Packaging Conference Exhibition, EMPC, 2019, pp. 1–4.

[9] N. Wang, Y. Liu, S. Chen, L. Ye, J. Liu, Highly thermal conductive and electrically insulated graphene based thermal interface material with long-term reliability, in: 2019 IEEE 69th Electronic Components and Technology Conference, ECTC, 2019, pp. 1564–1568.

[10] M.F. Abdullah, S.A. Mohamad Badaruddin, M.R. Mat Hussin, M.I. Syono, Evaluation on the reduced graphene oxide thermal interface material and heat spreader for thermal management in high-temperature power device, J. Teknologi 83 (3) (2021) 53–59, [Online]. Available: https://journals.utm.my/jurnalteknologi/article/view/15102.

[11] J.S. Lewis, Reduction of device operating temperatures with graphene-filled thermal interface materials, C 7 (3) (2021) [Online]. Available: https://www.mdpi.com/2311-5629/7/3/53.

[12] A.M. Hadi, M.A. Ismael, H.A. Alhattab, Improvement of heat sink performance using graphite and graphene coating, Basrah J. Eng. Sci. 21 (2021) [Online]. Available: http://dx.doi.org/10.33971/bjes.21.1.7.

[13] P. Zhang, N. Wang, C. Zandén, L. Ye, Y. Fu, J. Liu, Thermal characterization of power devices using graphene-based film, in: 2014 IEEE 64th Electronic Components and Technology Conference, ECTC, IEEE, 2014, pp. 459–463.

[14] H.S. Seo, D. Shin, Development of parallel and direct cooling system for EV/FCEV inverter, in: SAE Technical Paper, SAE International, 2018.

[15] G. Tang, T.c. Chai, X. Zhang, Thermal optimization and characterization of SiC-based high power electronics packages with advanced thermal design, IEEE Trans. Compon. Packag. Manuf. Technol. 9 (5) (2019) 854–863.

[16] A. Bryant, N.-A. Parker-Allotey, D. Hamilton, I. Swan, P.A. Mawby, T. Ueta, T. Nishijima, K. Hamada, A fast loss and temperature simulation method for power converters, Part I: Electrothermal modeling and validation, IEEE Trans. Power Electron. 27 (1) (2012) 248–257.
[17] A.H. Mohamed, H. Vansompel, P. Sergeant, Electrothermal design of a discrete gan-based converter for integrated modular motor drives, IEEE J. Emerg. Sel. Top. Power Electron. 9 (5) (2021) 5390–5406.
[18] UN Sustainable transport, 2021, Available at https://sdgs.un.org/topics/sustainable-transport. (Accessed 16 December 2021).
[19] Wolfspeed. Power and R.F. CAB450M12XM3. [Online]. Available: https://assets.wolfspeed.com/uploads/2020/12/CAB450M12XM3.pdf.
[20] S. Amirpour, T. Thiringer, D. Hagstedt, Power loss analysis in a SiC/IGBT propulsion inverter including blanking time, mosfet's reverse conduction and the effect of thermal feedback using a PMSM model, in: IECON 2020 the 46th Annual Conference of the IEEE Industrial Electronics Society, 2020, pp. 1424–1430.
[21] C. Zhang, S. Srdic, S. Lukic, Y. Kang, E. Choi, E. Tafti, A SiC-based 100 kW high-power-density (34 kW/L) electric vehicle traction inverter, in: 2018 IEEE Energy Conversion Congress and Exposition, ECCE, 2018, pp. 3880–3885.
[22] T.M. Jahns, G.B. Kliman, T.W. Neumann, Interior permanent-magnet synchronous motors for adjustable-speed drives, IEEE Trans. Ind. Appl. IA-22 (4) (1986) 738–747.
[23] M. Meyer, J. Bocker, Optimum control for interior permanent magnet synchronous motors (IPMSM) in constant torque and flux weakening range, in: 12th International Power Electronics and Motion Control Conference, 2006, pp. 282–286.
[24] A. Acquaviva, T. Thiringer, Energy efficiency of a SiC MOSFET propulsion inverter accounting for the MOSFET's reverse conduction and the blanking time, in: 2017 19th European Conference on Power Electronics and Applications, EPE'17 ECCE Europe, 2017, pp. P.1–P.9.
[25] ENGYS ltd, 2021, Available at https://engys.com. (Accessed 13 November 2021).
[26] Wolfspeed. Power and R.F. CAS300M12BM2. [Online]. Available: https://assets.wolfspeed.com/uploads/2020/12/cas300m12bm2.pdf.
[27] A.V. Girão, G. Caputo, M.C. Ferro, Chapter 6 - Application of scanning electron microscopy–Energy dispersive X-Ray spectroscopy (SEM-EDS), in: T.A. Rocha-Santos, A.C. Duarte (Eds.), Characterization and Analysis of Microplastics, in: Comprehensive Analytical Chemistry, vol. 75, Elsevier, 2017, pp. 153–168, [Online]. Available: https://www.sciencedirect.com/science/article/pii/S0166526X16301519.
[28] T. Hitachi, H. Gohara, F. Nagaune, Direct liquid cooling IGBT module for automotive applications, Fuji Electric Rev. 58 (2) (2012) 55–59.
[29] K. Olesen, R. Bredtmann, R. Eisele, "ShowerPower" new cooling concept for automotive applications, 2006, [Online]. Available: https://api.semanticscholar.org/CorpusID:113502569.
[30] Y. Li, Implementation of multiple time steps for the multi-physics solver based on chtMultiRegionFoam., in: Proceedings of CFD with OpenSource Software, 2016, Edited By Nilsson. H., 2016.
[31] CFDdirect, Energy equation in openfoam, 2021, Available at https://cfd.direct/openfoam/energy-equation/. (Accessed 25 November 2021).
[32] openfoamwiki, chtMultiRegionFoam, 2021, Available at https://openfoamwiki.net/index.php/ChtMultiRegionFoam. (Accessed 25 November 2021).
[33] OpenFOAM, 2021, Available at https://openfoam.org/. (Accessed 13 November 2021).
[34] N.-J. Song, C.-M. Chen, C. Lu, Z. Liu, Q.-Q. Kong, R. Cai, Thermally reduced graphene oxide films as flexible lateral heat spreaders, J. Mater. Chem. A 2 (2014) 16563–16568.
[35] Z. Liu, Z. Li, Z. Xu, Z. Xia, X. Hu, L. Kou, L. Peng, Y. Wei, C. Gao, Wet-spun continuous graphene films, Chem. Mater. 26 (23) (2014) 6786–6795.
[36] Tailoring the thermal and electrical transport properties of graphene films by grain size engineering, Nature Commun. 8.
[37] H. Becerril, J. Mao, Z. Liu, R. Stoltenberg, Z. Bao, Y. Chen, ACS, Nano 2 (2009) 463, (2008).
[38] Z. Wei, Z. Ni, K. Bi, M. Chen, Y. Chen, In-plane lattice thermal conductivities of multilayer graphene films, Carbon 49 (8) (2011) 2653–2658, [Online]. Available: https://www.sciencedirect.com/science/article/pii/S0008622311001576.
[39] H. Han, Y. Zhang, N. Wang, M.K. Samani, Y. Ni, Z.Y. Mijbil, M. Edwards, S. Xiong, K. Sääskilahti, M. Murugesan, Y. Fu, L. Ye, H. Sadeghi, S. Bailey, Y.A. Kosevich, C.J. Lambert, J. Liu, S. Volz, Functionalization mediates heat transport in graphene nanoflakes, Nature Commun. 7 (1) (2016).
[40] A.M. Hadi, M.A. Ismael, H.A. Alhattab, Improvement of heat sink performance using graphite and graphene coating, Basrah J. Eng. Sci. 21 (1) (2021) 50–55.
[41] CO2 Intensity of Electricity Generation, 2021, Available at https://www.eea.europa.eu/data-and-maps/data/co2-intensity-of-electricity-generation. (Accessed 16 December 2021).
[42] G. Mademlis, N. Sharma, Y. Liu, J. Tang, Zero-sequence current reduction technique for electrical machine emulators with DC-coupling by regulating the SVM zero states, IEEE Trans. Ind. Electron. (2021) 1.